Heliyon 9 (2023) e18003

Contents lists available at ScienceDirect

Heliyon

journal homepage: www.cell.com/heliyon

Darcy flow of convective and radiative Maxwell nanofluid over a porous disk with the influence of activation energy

Muhammad Naveed Khan [a], Abdul Hafeez [b,*], Showkat Ahmed Lone [c], Salmeh A. Almutlak [c], Ibrahim E. Elseey [d]

[a] School of Energy and Power Engineering, Jiangsu University, PO Box 28, Zhenjiang, Jiangsu, 212013, China
[b] Department of Mathematics, University of Loralai, Loralai, Pakistan
[c] Department of Basic Sciences, College of Science and Theoretical Studies, Saudi Electronic University, Riyadh, 11673, Kingdom of Saudi Arabia
[d] Mechanical Engineering Department, College of Engineering, King Khalid University, Abha, 61421, Saudi Arabia

ARTICLE INFO

Keywords:
Maxwell nanofluid
Darcy law
Activation energy
Covective boundary condition
Heat source/sink
Thermal radiation

ABSTRACT

This study reveals an incompressible steady Darcy flow of Maxwell nanofluid by a porous disk with the impact of activation energy. The liquid flow is due to a stretchable rotating disk. The heat equation also includes the impact of heat source/sink and radiation for the purpose of heat transportation. The von Karman transformations are utilized to gain the dimensionless form of ordinary differential equations (ODEs). The solutions are visualised in the form of graphical results using bvp 4c method in Matlab software. The ranges of the associated physical parameters as, $0.0 \le \beta \le 0.9$, $0.0 \le M \le 0.9$, $0.0 \le \lambda \le 1.5$, $0.1 \le R \le 0.9$, $-0.2 \le s \le 1.3$, $0.3 \le B_i \le 0.6$, $0.0 \le \gamma \le 0.15$, $0.1 \le Nt \le 2.0$, $0.2 \le Nb \le 0.8$, $0.0 \le Rd \le 0.3$, $0.0 \le \sigma \le 1.5$, and $0.0 \le E \le 0.9$ are provided for the graphical solutions developed for the problem. The data of Nusset1 and Sherwood numbers are presented here with regard to various physical parameters. According to the numerical results, increasing the Deborah number has a trend to decrease the radial curves. Moreover, the temperature distribution is increased considerably for rising the radiation parameter and the higher rate of the rotation parameter shows a weaker concentration trend. To validate the numerical approach, an excellent comparison is established using a tabular description. To sum up, the current study effectively fills a gap in the antecedent literature.

1. Introduction

Fluids with non-Newtonian behavior have been used in a variety of engineering applications, including remediation, hydraulic fracturing and a variety of industrial processes. Non-Newtonian fluids have flow equations that are far more nonlinear than the Navier-Stokes equations. Three categories—rate, differential and integral—are used to categorise these non-Newtonian fluid models. The present model, known as the Maxwell fluid model, is a subclass of a rate type liquid model that is being taken into consideration and predicts the effects of relaxation time. Mabood et al. [1] discussed the convective Maxwell liquid flow with the effect of thermal radiation. Moreover, the non-Newtonian Maxwell fluid flow with the presence of nanoparticles was explored by Ijaz and Ayub [2]. The Cattaneo-Christov theory on Maxwell nanofluid flow was discussed by Ahmed et al. [3]. In their study, they used a rotating disk geometry to generate the liquid flow. The rotating flow of Maxwell nanofluid was deliberated by Maboob et al. [4] and obtained

* Corresponding author.
E-mail address: ahafeez@math.qau.edu.pk (A. Hafeez).

https://doi.org/10.1016/j.heliyon.2023.e18003
Received 21 February 2023; Received in revised form 3 July 2023; Accepted 5 July 2023
Available online 13 July 2023

Nomenclature

r, φ and z	Cylindrical coordinate
ν	kinematic viscosity
σ_1	electrical conductivity
c_p	specific heat capacity
λ_1	relaxation time
D_B	the Brownian diffusion coefficient
k^*	Stefan-Boltzmann constant
η	dimensionless variable
E_a	activation energy
n	filter rate constant
B_0	Magnetic filed strength
Ω	Swirl rate of the disk
T_f	convective fluid temperature
C_w	wall concentration
K	permeability of medium
R	stretching parameter
M	magnetic parameter
Nb	Brownian motion parameter
Rd	Raditation parameter
δ	temperature difference parameter
E	activation energy parameter
$\Pr$	Prandtl number
θ_w	temperature ratio parameter
Sh_r	Sherwood number
F	radial velocity
ϕ	Dimensionless concentration
H	Axial velocity
u, v and w	Velocity components
ρ	fluid density
μ	dynamic viscosity
k	thermal conductivity
h_f	convective heat transfer coefficient
τ	heat capacities ratio
σ^*	Rosseland mean spectral absorption coefficient
D_T	the thermal diffusion coefficient
k_1	Boltzmann constant
K_r	reaction rate
w_0	mass flux velocity
c	stretch rate of the disk
T_∞	far away fluid temperature
C_∞	far away concentration
s	suction parameter
λ	porosity parameter
β	relaxation time parameter
B_i	Biot number
Sc	Schmidt number
Rd	radiation parameter
σ	chemical reaction parameter
γ	heat generation parameter
Nt	thermophoresis parameter
Nu_r	Nusselt number
$'$	differentiation with respect to η
θ	Dimensionless temperature
G	Azimuthal velocity

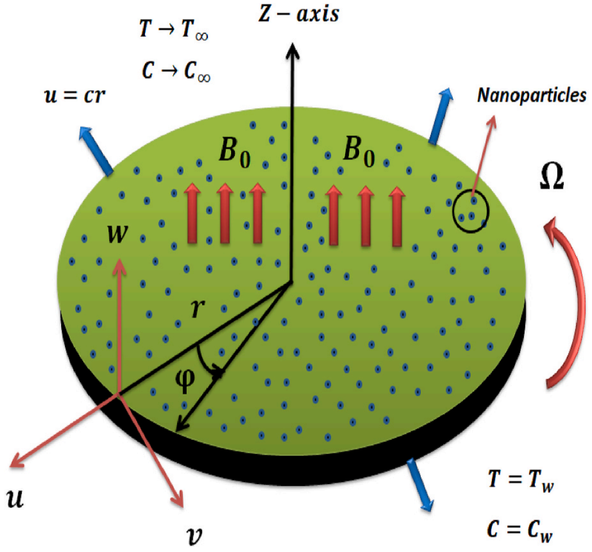

Fig. 1. aA physical diagram of the disk.

numerical solution. A number of applications have led many investigators to focus on the analysis of Maxwell flow [5–8].

According to the aforementioned literature study, it is evident that no researchers have looked into Maxwell fluid flow with these physical features that are included in the current problem. The key objective of this research is to study the investigation of Darcy flow of convective and radiative Maxwell nanofluid over a porous disk with the impact of activation energy. The governing problem is handled with a numerical method. The solutions are represented through graphical format and explained in detail.

2. Modeling of the problem

Let us assume an axisymmetric steady incompressible radiative Maxwell nanofluid flow by a rotating disk [9–22] with the role of Darcy effect. In addition, the heat and mass transportation are also discussed with the influence of heat source/sink, thermal radiation and activation energy [23], respectively. Further, the convective boundary condition [24] is also taken into consideration. A Buongiorno model is appropriate and adopted to discuss the thermophoresis and Brownian motion impacts. Here we assumed that the surface (disk) is porous with mass flux velocity w_0. The swirl and stretch rates of the disc are indicated here by (Ω,c), respectively. Fig. 1 (a) depicts the underlying geometry of the problem. In addition, (T_f, T_∞) the convective and far away fluid temperature, respectively. Moreover, (C_w, C_∞) are the wall and far away concentration, respectively.

In light of the aforementioned presumptions, the constructed equations are [3,25].

$$\frac{\partial u}{\partial r}+\frac{u}{r}+\frac{\partial w}{\partial z}=0, \tag{1}$$

$$u\frac{\partial u}{\partial r}-\frac{v^2}{r}+w\frac{\partial u}{\partial z}=\nu\frac{\partial^2 u}{\partial z^2}-\frac{\sigma_1}{\rho}{B_0}^2\left[u+\lambda_1 w\frac{\partial u}{\partial z}\right]-\frac{\varphi_1\nu}{K}u$$
$$-\lambda_1\left[u^2\frac{\partial^2 u}{\partial r^2}+w^2\frac{\partial^2 u}{\partial z^2}+2uw\frac{\partial^2 u}{\partial r\partial z}-\frac{2uv}{r}\frac{\partial v}{\partial r}-\frac{2vw}{r}\frac{\partial v}{\partial z}+\frac{uv^2}{r^2}+\frac{v^2}{r}\frac{\partial u}{\partial r}\right], \tag{2}$$

$$u\frac{\partial v}{\partial r}+\frac{uv}{r}+w\frac{\partial v}{\partial z}=\nu\frac{\partial^2 v}{\partial z^2}-\frac{\sigma_1}{\rho}{B_0}^2\left[v+\lambda_1 w\frac{\partial v}{\partial z}\right]-\frac{\varphi_1\nu}{K}v$$
$$-\lambda_1\left[u^2\frac{\partial^2 v}{\partial r^2}+w^2\frac{\partial^2 v}{\partial z^2}+2uw\frac{\partial^2 v}{\partial r\partial z}+\frac{2uv}{r}\frac{\partial u}{\partial r}+\frac{2vw}{r}\frac{\partial u}{\partial z}-2\frac{u^2 v}{r^2}-\frac{v^3}{r^2}+\frac{v^2}{r}\frac{\partial v}{\partial r}\right], \tag{3}$$

$$u\frac{\partial T}{\partial r}+w\frac{\partial T}{\partial z}=\frac{k}{\rho c_p}\left(\frac{\partial^2 T}{\partial z^2}\right)-\tau\left(\frac{D_T}{T_\infty}\left(\frac{\partial T}{\partial z}\right)^2+D_B\frac{\partial T}{\partial z}\frac{\partial C}{\partial z}\right)-\frac{1}{\rho c_p}\frac{\partial q_r}{\partial z}+\frac{Q(T-T_\infty)}{\rho c_p}, \tag{4}$$

$$u\frac{\partial C}{\partial r}+w\frac{\partial C}{\partial z}=D_B\frac{\partial^2 C}{\partial z^2}+\frac{D_T}{T_\infty}\frac{\partial^2 T}{\partial z^2}-K_r^2\left(\frac{T}{T_\infty}\right)^n exp\left(\frac{-E_a}{k_1 T}\right)(C-C_\infty), \tag{5}$$

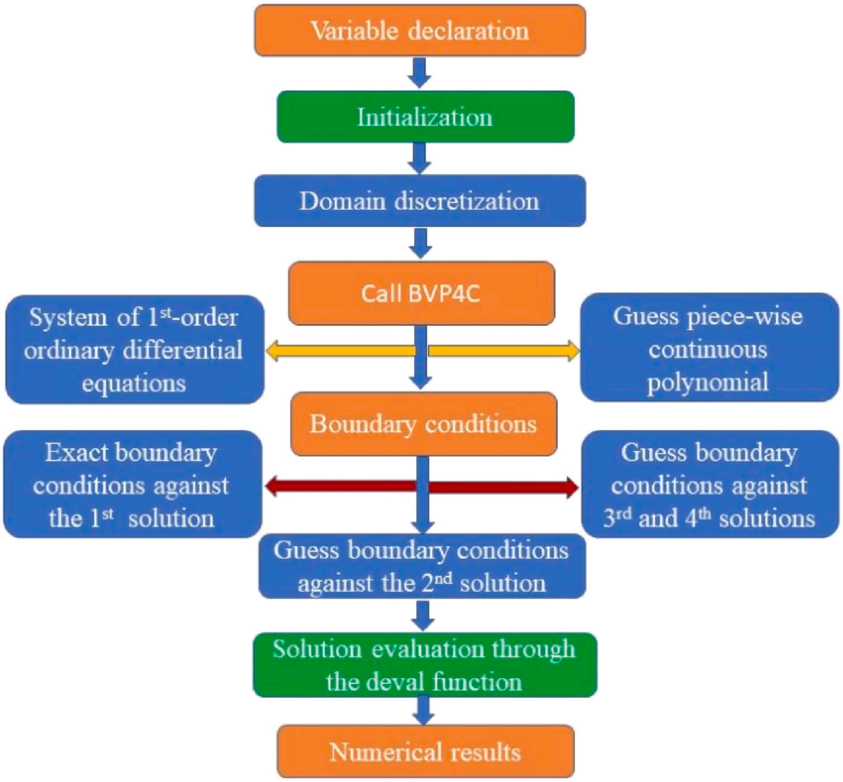

Fig. 1. bFlow chart diagram.

Table 1
Comparison table of $F'(0)$ and $G'(0)$ for various estimation of M, when $\beta = 0$.

$F'(0)$			
M	Ref. [29]	Ref. [30]	Current results
0.0	0.510233	0.510233	0.510232
0.1	0.480481	0.480481	0.480479
0.2	0.453130	0.453130	0.453135
$-G'(0)$			
M	Ref. [29]	Ref. [30]	Current results
0.0	0.615926	0.615926	0.615922
0.1	0.662122	0.662122	0.662131
0.2	0.708778	0.708778	0.708780

Table 2
Comparison table of $-\theta'(0)$ and $-\phi'(0)$ for various estimation of M, when $\beta = 0$.

$-\theta'(0)$			
M	Ref. [29]	Ref. [30]	Current results
0.0	0.325912	0.325912	0.325915
0.1	0.304612	0.304612	0.304609
0.2	0.283159	0.283159	0.283161
$-\phi'(0)$			
M	Ref. [29]	Ref. [30]	Current results
0.0	0.233494	0.233494	0.233486
0.1	0.215631	0.215631	0.215635
0.2	0.196521	0.196521	0.196519

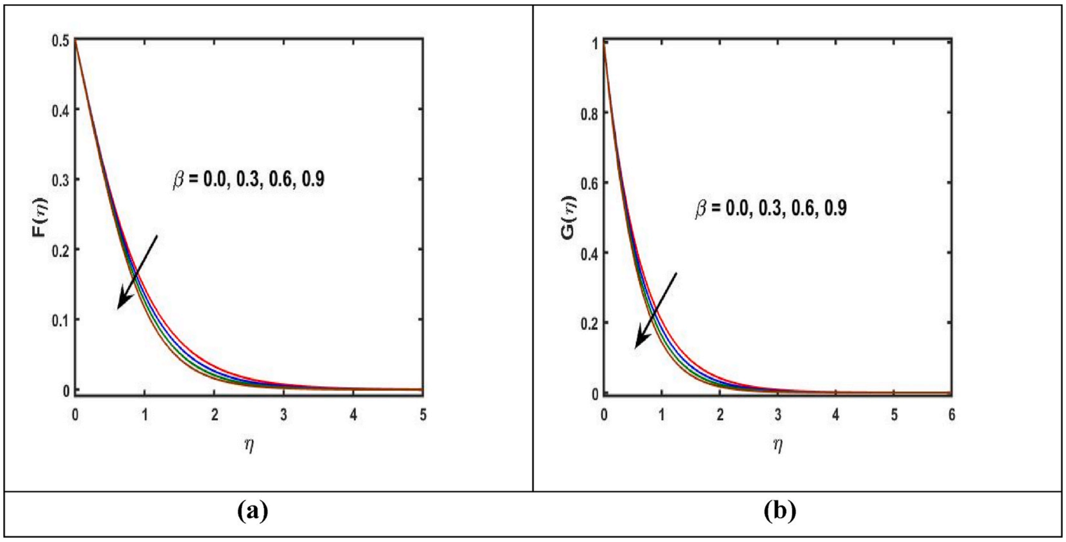

Fig. 2. a), b): lots of $F(\eta)$ and $G(\eta)$ by β.

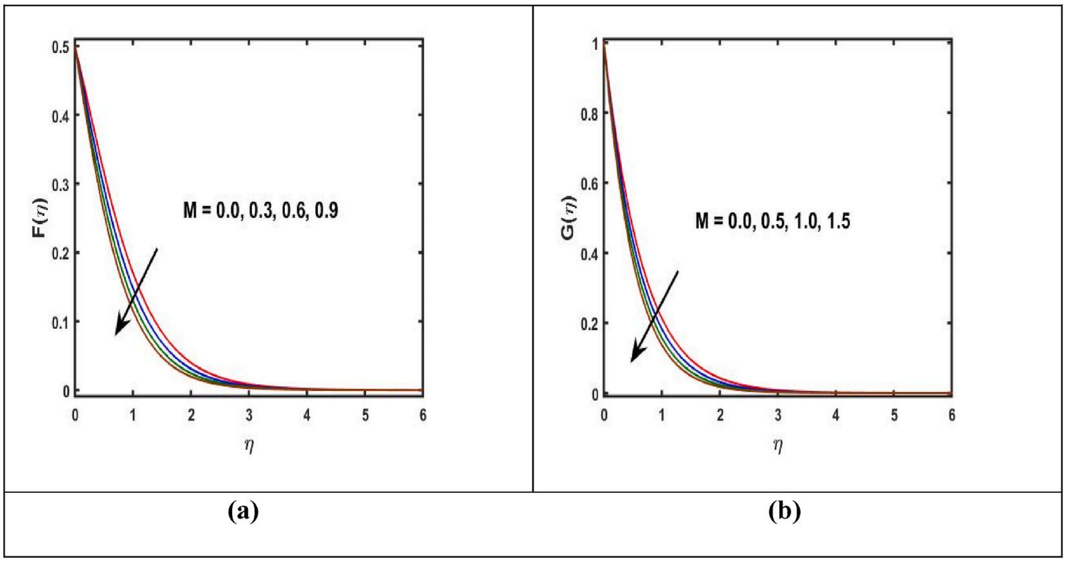

Fig. 3. a), b): Plots of $F(\eta)$ and $G(\eta)$ by M.

The boundary conditions are [26].

$$u = cr, v = \Omega \mathrm{r}, \mathrm{w} = w_0, \ -k\frac{\partial T}{\partial z} = h_f\left(T_f - T\right), C = C_w \text{ at } \quad z = 0,$$

$$u \to 0, v \to 0, T \to T_\infty, C \to C_\infty \ \ as \ \ z \to \infty \tag{6}$$

The radiative heat flux expression [26–28] is given by

$$q_r = -\frac{4}{3}\frac{\sigma^*}{k^*}\frac{\partial T^4}{\partial z} = -\frac{16}{3}\frac{\sigma^* T^3}{k^*}\frac{\partial T}{\partial z}, \tag{7}$$

The transformations is given by [26].

$$\eta = \sqrt{\frac{\Omega}{\nu}}z, u = \Omega r F, v = \Omega r G, w = \sqrt{\Omega \nu} H, \theta = \frac{T - T_\infty}{T_f - T_\infty}, \varphi = \frac{C - C_\infty}{C_w - C_\infty}. \tag{8}$$

Placing the variables (8) into Eqs. (1)–(5), results the following [3,25,28].

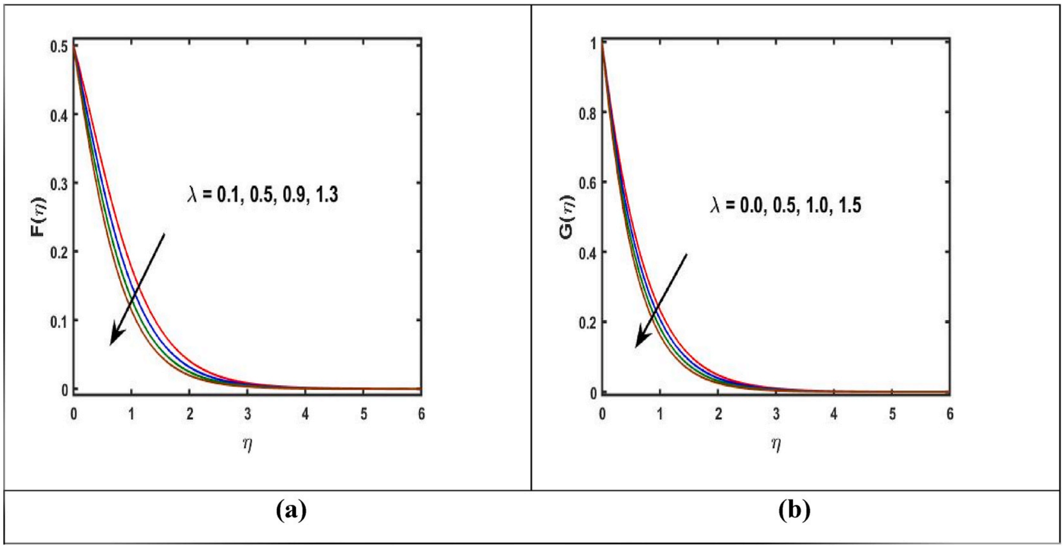

Fig. 4. a), b): Plots of $F(\eta)$ and $G(\eta)$ by λ.

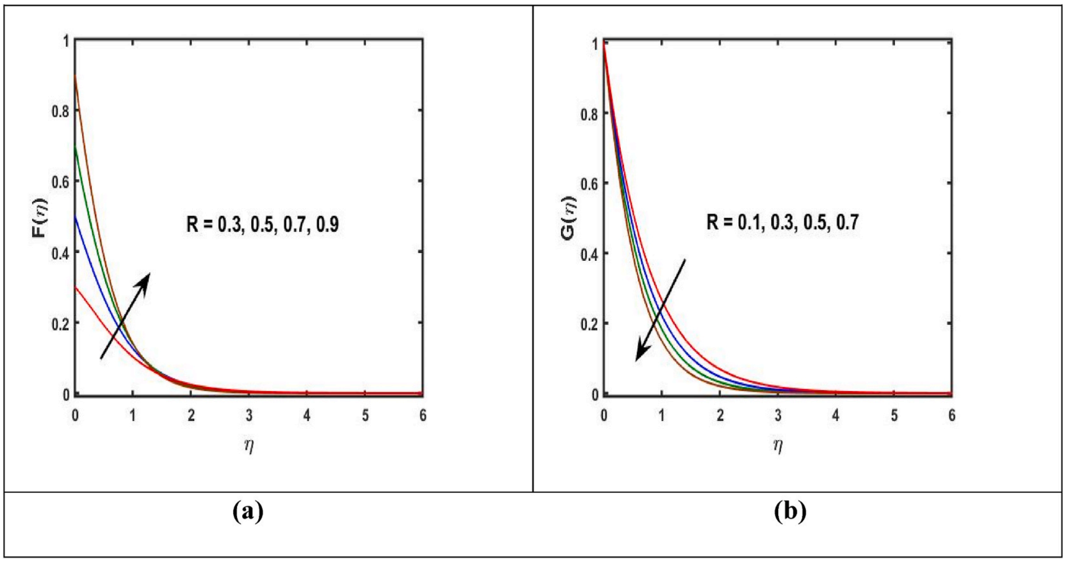

Fig. 5. a), b): Plots of $F(\eta)$ and $G(\eta)$ by R.

$$H' + 2F = 0, \tag{9}$$

$$F^2 - G^2 + F'H - F'' + \beta_1\left(F''H^2 + 2FF'H - 2GG'H\right) + \lambda F + M(F + \beta_1 F'H) = 0, \tag{10}$$

$$2FG + G'H - G'' + \beta_1\left(G''H^2 + 2(FG' + F'G)H\right) + \lambda G + M(G + \beta_1 G'H) = 0, \tag{11}$$

$$\theta''\left(1 + \frac{4}{3}Rd\right) + \frac{4}{3}Rd\left[\begin{array}{c}\left(\theta^3\theta'' + 3\theta^2\theta'^2\right)(\theta_w - 1)^3 \\ +3\left(\theta^2\theta'' + 2\theta\theta'^2\right)(\theta_w - 1)^2 + 3\left(\theta\theta'' + \theta'^2\right)(\theta_w - 1)\end{array}\right]$$

$$-\Pr H\theta' + \Pr\left(Nb\theta'\varphi' + Nt\theta'^2\right) + \gamma \Pr \theta = 0, \tag{12}$$

$$\phi'' - ScH\varphi' + \frac{Nt}{Nb}\theta'' - ScR\sigma(1 + \delta\theta)^n exp\left(\frac{-E}{1 + \delta\theta}\right)\phi = 0. \tag{13}$$

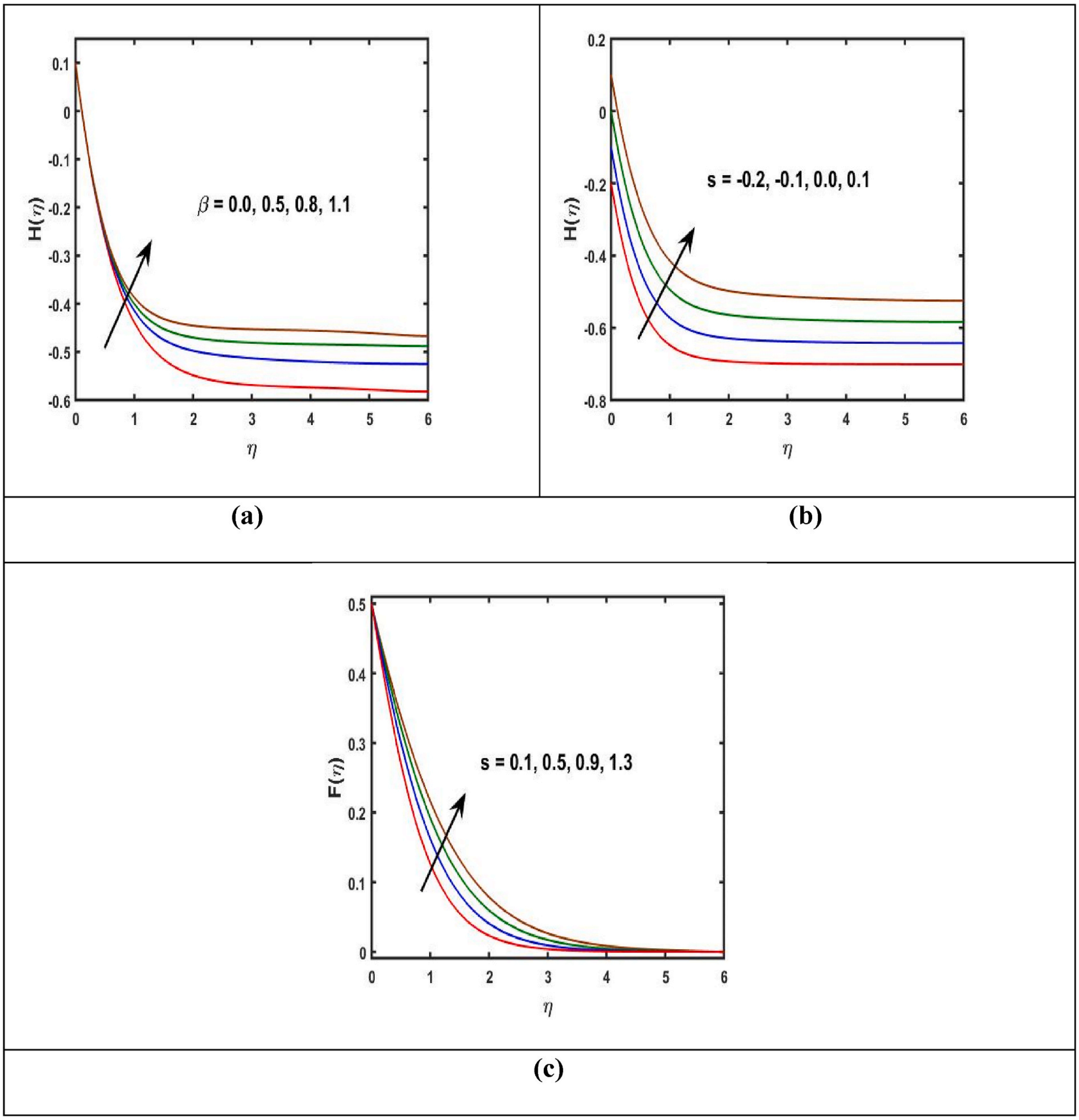

Fig. 6. a), 6b): Plots of $H(\eta)$ by β and s. **c):** Plot of $F(\eta)$ by s.

The transformed BCs are [26].

$$F(\eta) = R, G(\eta) = 1, H(\eta) = s, \theta^{'}(\eta) = -Bi(1-\theta(\eta)), \phi(\eta) = 1 \text{ at } \eta = 0,$$

$$F(\eta)\to 0, G(\eta)\to 0, \theta(\eta)\to 1, \phi(\eta)\to 0 \text{ as } \eta\to\infty, \tag{14}$$

Here, $s = \left(\frac{w_0}{\sqrt{\Omega\nu}}\right)$ is the suction parameter, $\beta_1 = (\lambda_1\Omega)$ the relaxation time parameter, $M = \left(\frac{\sigma_{1B_0^2}}{\rho\Omega}\right)$ the magnetic field parameter, $R = \left(\frac{c}{\Omega}\right)$ the stretching parameter, $\lambda = \left(\frac{\nu\varphi_1}{K\Omega}\right)$ the porosity parameter, $Nt = \left(\frac{\tau D_T(T_f - T_\infty)}{\nu T_\infty}\right)$ the thermophoresis parameter, $Nb = \left(\frac{\tau D_B(C_w - C_\infty)}{\nu}\right)$ the Brownian motion parameter, $Bi = \left(\frac{h_f}{k}\sqrt{\frac{\nu}{\Omega}}\right)$ the Biot number, $E = \left(\frac{E_a}{k_1 T_\infty}\right)$ the activation energy, $\gamma = \left(\frac{Q}{\rho c_p\Omega}\right)$ the heat generation parameter, $\delta = \left(\frac{T_f - T_\infty}{T_\infty}\right)$ the temperature difference parameter, $\sigma = \left(\frac{K_r^2}{c}\right)$ the reaction parameter, $\theta_w = \left(\frac{T_w}{T_\infty}\right)$ the temperature ratio

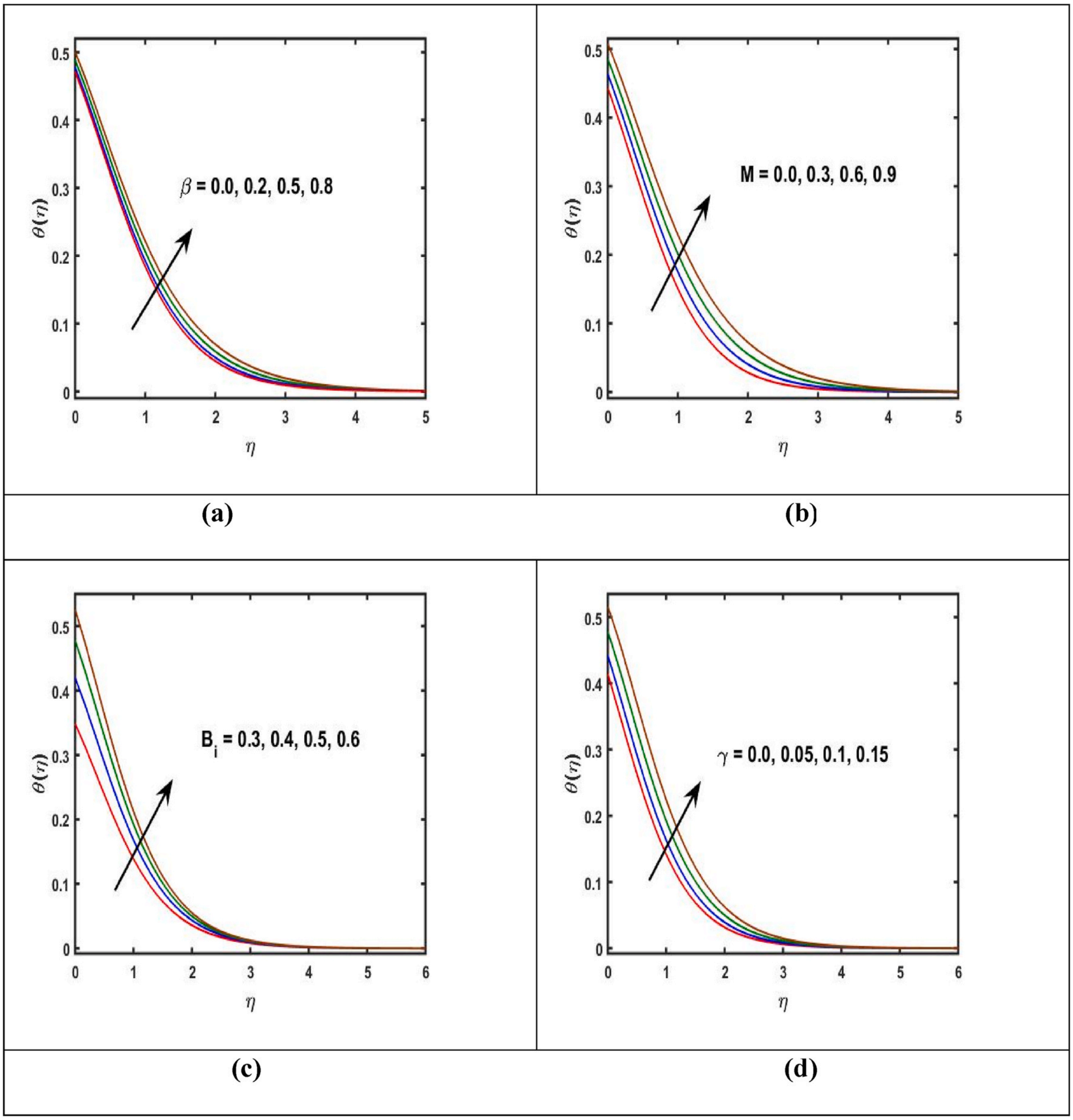

Fig. 7. a), b): Plots of $\theta(\eta)$ by β and M. c), d): Plots of $\theta(\eta)$ by B_i and γ.

parameter, $Rd = \left(\frac{16}{3}\frac{\sigma^* T_\infty^3}{kk^*}\right)$ the radiation parameter, $Sc = \left(\frac{\nu}{D_B}\right)$ the Schmidt number and $\Pr = \frac{\nu(\rho c_p)}{k}$ the Prandtl number.

The Nusselt $\{Nu_r\}$ and Sherwood $\{Sh_r\}$ numbers are defined by [28]

$$Nu_r = -\left(1 + \frac{16}{3}\frac{\sigma^* T^3}{kk^*}\right)\frac{r\left(\frac{\partial T}{\partial z}\right)_{z=0}}{\left(T_f - T_\infty\right)}, Sh_r = \frac{rD_B\left(\frac{\partial C}{\partial z}\right)_{z=0}}{D_B(C_w - C_\infty)}. \tag{15}$$

The dimensionless form are

$$Re^{-\frac{1}{2}}Nu_r = -\left\{1 + \frac{4Rd}{3}[1 + (\theta_w - 1)\theta(0)]^3\right\}\theta'(0), Re^{-\frac{1}{2}}Sh_r = -\phi'(0), \tag{16}$$

Where the Reynold number is $Re = \left(\frac{r^2\Omega}{\nu}\right)$.

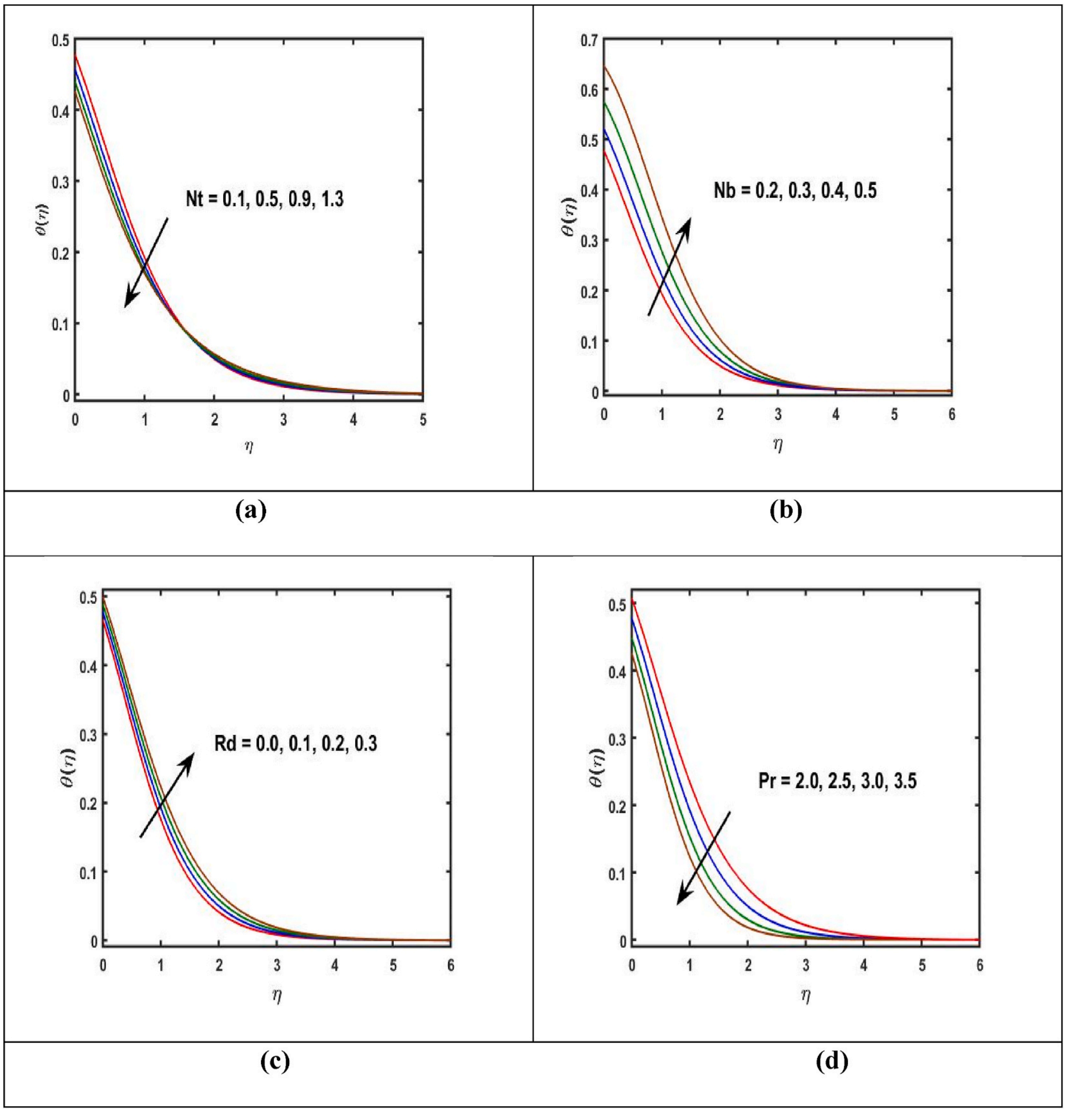

Fig. 8. a), b): Plots of $\theta(\eta)$ by *Nt* and *Nb*. c), d): Plot of $\theta(\eta)$ by *Rd* and *Pr*.

2.1. Numerical scheme

The current problem solution has been obtained by the aid of Bvp4c Matlab approach numerically. To use this approach first we convert ODEs into the system of 1st order differential equations, which is followed by Eqs. (17)-(22). Aditionally, the flow chart for bvp4c techniquie is given in Fig. 1(b).

$$\begin{pmatrix} \varsigma_1 = H \\ \varsigma_2 = F \\ \varsigma_3 = F^{'} \\ \varsigma_4 = G \\ \varsigma_5 = G^{'} \\ \varsigma_6 = \theta \\ \varsigma_7 = \theta^{'} \\ \varsigma_8 = \phi \\ \varsigma_9 = \phi^{'} \end{pmatrix}, \tag{17}$$

$$\varsigma\varsigma_1 = -2\varsigma_2, \tag{18}$$

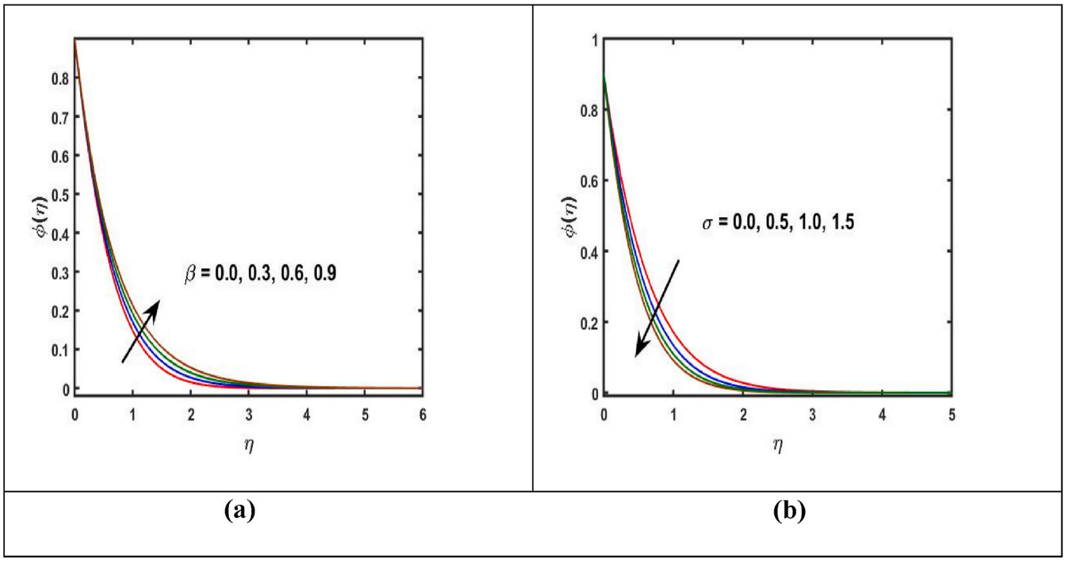

Fig. 9. a), b): Plots of $\varphi(\eta)$ by β and σ.

$$\varsigma\varsigma_2 = \left(\frac{1}{1-\beta_1\varsigma_1{}^2}\right)\begin{bmatrix} \varsigma_4{}^2 - \varsigma_2{}^2 - \varsigma_1\varsigma_3 - 2\beta_1\varsigma_1\varsigma_2\varsigma_3 - \lambda\varsigma_2 \\ +2\beta_1\varsigma_1\varsigma_4\varsigma_5 - M(\varsigma_2 + \beta_1\varsigma_1\varsigma_3) \end{bmatrix}, \tag{19}$$

$$\varsigma\varsigma_3 = \left(\frac{1}{1-\beta_1\varsigma_1{}^2}\right)\begin{bmatrix} 2\varsigma_2\varsigma_4 + \varsigma_1\varsigma_5 - 2\beta_1\varsigma_1(\varsigma_2\varsigma_5 + \varsigma_3\varsigma_4) + \lambda\varsigma_4 \\ +M(\varsigma_4 + \beta_1\varsigma_1\varsigma_5) \end{bmatrix}, \tag{20}$$

$$\varsigma\varsigma_4 = \begin{pmatrix} 1 + \frac{4}{3}Rd + \frac{4}{3}Rd\varsigma_6{}^3(\theta_w - 1)^3 \\ +4Rd\varsigma_6(\theta_w - 1)[(\theta_w - 1)\varsigma_6 + 1] \end{pmatrix}^{-1} \begin{pmatrix} \Pr(\varsigma_1\varsigma_7 - Nb\varsigma_7\varsigma_9 - Nt\varsigma_7{}^2 - \gamma\varsigma_6) \\ -4Rd(\theta_w - 1)\varsigma_7{}^2\left[\varsigma_6{}^2(\theta_w - 1)^2 + 2\varsigma_6(\theta_w - 1) + 1\right] \end{pmatrix}, \tag{21}$$

$$\varsigma\varsigma_5 = Sc\left(\varsigma_1\varsigma_9 + \sigma R(1+\delta\varsigma_6)^n Exp\left(\frac{-E}{1+\delta\varsigma_6}\right)\varsigma_8\right) - \frac{Nt}{Nb}\,\varsigma\varsigma_4. \tag{22}$$

The non-dimensionalized form of the boundary conditions is

$$\left\{\begin{matrix} \varsigma_1(0) = s, \varsigma_2(0) = R, \varsigma_4(0) = 1, \varsigma_7(0) = -Bi(1-\varsigma_6(0)), \varsigma_8(0) = 1 \\ \varsigma_2(\infty)\to 0, \varsigma_4(\infty)\to 0, \varsigma_6(\infty)\to 0, \varsigma_8(\infty)\to 0 \end{matrix}\right\}. \tag{23}$$

3. Result and discussion

In this part of the research, the objective is to investigate the physical significance of several emerging parameters on the fluid velocity, thermal, and concentration of the liquid under study.

The physical results are acquired by using bvp4c Matlab solution tenchique. Moreover, the tabluted values for the heat and mass transfer rate are observed and comparisons are done with pervious published data. The eveloving parmeters like relaxation parameter (β), suction parameter (s), stretching parameter (R), porosity parameter (λ), (M), (Nb), Biot number (B_i), Raditation parameter (Rd), thermophoresis parameter (Nt), Schmidt number (Sc), temperature difference parameter (δ), radiation parameter (Rd), activation energy parameter (E), chemical reaction parameter (σ), heat generation parameter (γ) and (Pr) on the velocity, thermal, and concentration profiles are sketched.

Tables 1 and 2 is formed to compare the present results with previous published data which shows great harmony among them.

The variation of affecting parameter (β, M, λ, R and s) on the radial, angular, and axial velocities profiles are sketched in Figs. 2–6. It is illustrated from Fig. 2(a) and (b) that great estimation of β declines the radial as well as angular velocity of the liquid. Physically, for the larger values of β behave like a solid and for smaller values its behave like a fluid, thereby the fluid resistance improves which result to diminishes in both directions. Fig. 3(a) and (b) represents the behavior of M on the radial and angular velocity. As, due to lager estimation of magnetic effect, the resistive forces boost up as a results the fluid velocity declines along the radial and angular direction. The diversion in the velocity sketched for the various estimation of λ, is displayed in Fig. 4(a) and (b). It is discovered that the velocity of the liquid and associated boundary layer thickness decline due to higher values of λ. Actually, the occurrence of porous media produces the resistance to the motion of the liquid, which deteriorating the fluid velocity in both direction. The variation in the radial and angular velocity due to larger estimation of stretching ratio parameter (R) evaluated in Fig. 5(a) and (b). It is noted in Fig. 5(a) that

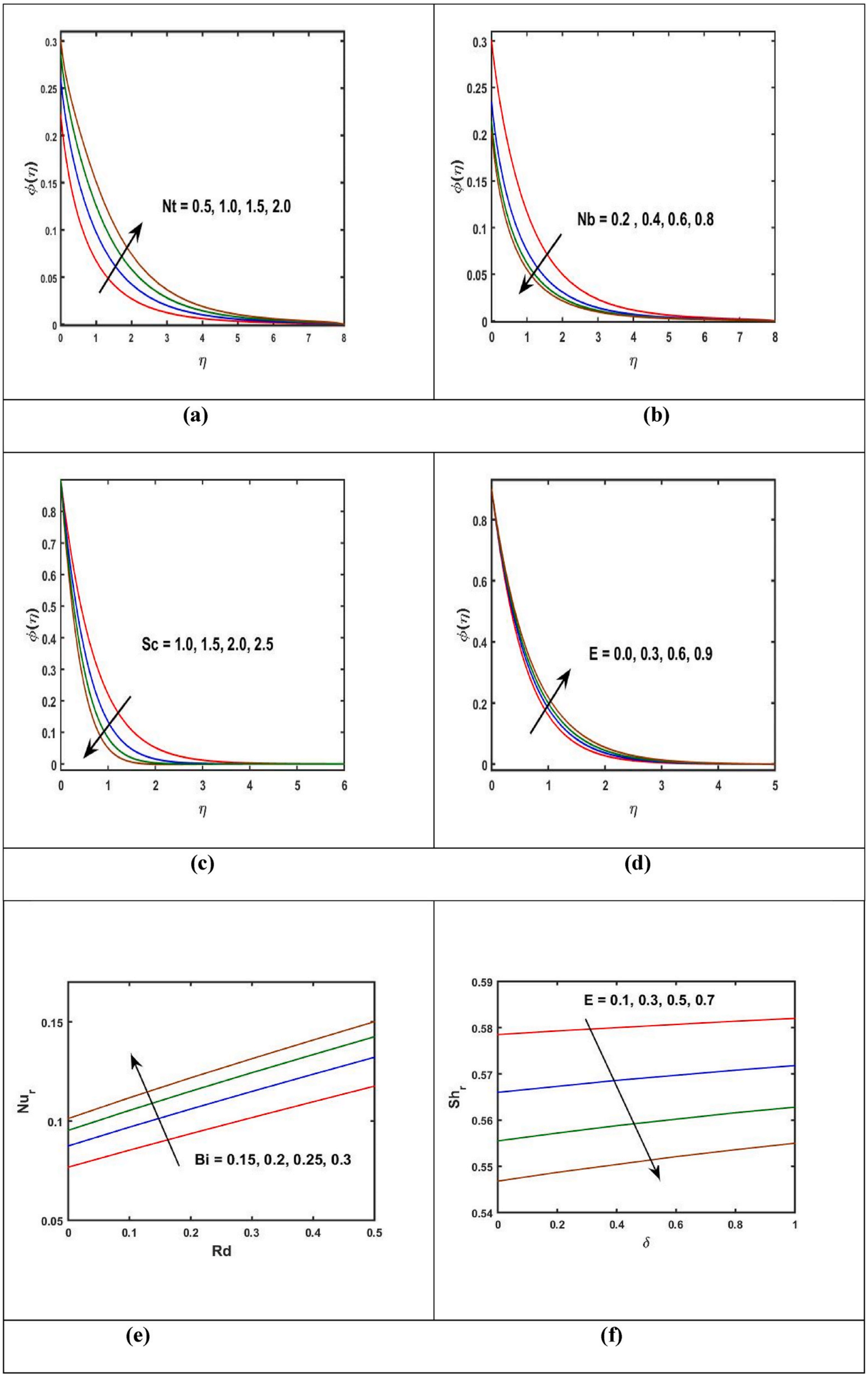

Fig. 10. a), b): Plots of $\phi(\eta)$ by Nt and Nb. c), d): Plots of $\phi(\eta)$ by Sc and E. e): Plot of Nu_r by Bi. f): Plots of Sh_r by E.

various estimation of R improves the fluid velocity in radial direction, while opposite trend is found in the case of angular velocity, which is depicted in Fig. 5(b). The upshot of relaxation and suction parameter against the axial velocity is shown in Fig. 6(a) and (b). It can be shown that by taking the bigger estimation of β and s, the fluid velocity in axial direction is improved with respect to both parameters. Fig. 6(c) depicts the variation in the fluid velocity due to various values s. As obvious from the curve that the improvement in fluid velocity and boundary layer thickness can be demonstrated by increasing s.

The outcomes of the developing parameters on the thermal profiles are depicted in the Figs. (7) and (8). It is showed from Fig. 7(a) and (b) that enlarging values of β and M boosts the liquid temperature and boundary layer become thicker due to higher resistive forces. The variation in $\theta(\eta)$ are sketched against the numerous values of B_i and γ and are illustrated in Fig. 7(c) and (d). It is seen from the sketch that greater estimation of B_i and γ improves the thermal profile. The higher values of Nt declines the temperature distribution, while converse trend is seen for Nb, which both are sketched in Fig. 8(a) and (b), respectively. Additionally, Fig. 8(c) and (d) depict the effect of (Rd) and (Pr) on the $\theta(\eta)$ sketch. It is further observed that higher estimation of Rd and Pr improves the temperature of the liquid. Physically, the occurrence of radiative heat flux shows more heat absorption in the liquid which boosts up the liquids temperature.

The impact of numerous parameter on $\varphi(\eta)$, sketch is portrayed in the Figs. (9) and (10). From Fig. 9(a) and (b), it is noted that due to larger estimation of relaxation parameter (β) and chemical reaction parameter (σ) the $\phi(\eta)$ sketch and related thickness of boundary layer enlarges β, while opposite trend is seen for the numerous values of σ. The diversion in the $\phi(\eta)$ sketch against the growing estimation of Nt and Nb is shown in Fig. 10(a) and (b). It is noted that due to larger values of Nt, the $\phi(\eta)$ sketch expands while opposite trend is observed for the bigger estimation of Nb. The effect of the Sc and E against the nanoparticles concentration profile is given in Fig. 10(a) and (b). It is described that nanoparticles concentration declines for the larger values of Sc, while converse trend is seen for the higher estimation of activation energy parameter. Physically, growing values of Sc causes a reduction in the mass diffusivity which leads to decay the $\phi(\eta)$ sketch and corresponding boundary layer thickness. Moreover due to larger E weaker reaction rate which rises the chemical reaction. Further, the effect of B_i and E on Nusselt as well as Sherwood numbers are drawn in Fig. 10(e) and (f). It is noted that the Nusselt number enhances by the higher rate of B_i and Rd. Additionally, the skin friction reduces with the impact of E.

4. Concluding remarks

The current investigation mainly focuses on the radiative Maxwell nanofluid flow with Darcy - Forchheimer across the porous medium subject to rotating disk. The heat and mass transport analysis is presented by the influence of nonlinear thermal radiation and activation energy. Moreover, convective boundary conditions with suction effect also take to analyze in the current investigation. The key finding of the current paper are followed as,

- The radial and angular velocities are reduced for larger estimation β, while axial velocity shows opposite trend for β.
- Due to appearance of porous media impact the resistance of fluid motion enhances, as a result the fluid vecloity declines.
- Higher estimation of suction parameter improves the radial and axial velocity.
- More heat is transmitted into the fluid due lager estismation of Rd, which results to improves the temperature.
- Larger values of magnetic parameter and Biot number develops the temperature of the liquid.
- The higher values of Brownian motion parameter improves the temperature profile but opposite trend is noted for concentration profile.
- The nanoparticle concentration is augmented by the growing estimation of E.
- As the Biot number and radiation parameter increase, so does the rate of heat transfer.
- The skin friction is reduced with the influence of activation energy.

Author contribution statement

Muhammad Naveed Khan: Conceived and designed the analysis; Wrote the paper.
Abdul Hafeez: Analyzed and interpreted the data; Wrote the paper.
Haifaa F Alrihieli: Contributed analysis tools or data; Wrote the paper.
Showkat Ahmed Lone, Salmeh A. Almutlak, Ibrahim E. Elseey: Analyzed and interpreted the data; Contributed analysis tools or data; Wrote the paper.

Data availability statement

Data will be made available on request.

Declaration of competing interest

The authors declare that they have no known competing financial interests or personal relationships that could have appeared to influence the work reported in this paper

Acknowledgment

The authors extend their appreciation to the Deanship of Scientific Research at King Khalid University for funding this work through large group Research Project under grant number RGP2/153/44.

References

[1] F. Mabood, M. Imtiaz, T. Hayat, A. Alsaedi, Unsteady convective boundary layer flow of Maxwell fluid with nonlinear thermal radiation: a numerical study, Int. J. Nonlinear Sci. Numer. Stimul. 17 (2016) 221–229.
[2] M. Ijaz, M. Ayub, Nonlinear convective stratified flow of Maxwell nanofluid with activation energy, Heliyon 5 (2019), e01121.
[3] A. Ahmed, M. Khan, J. Ahmed, A. Hafeez, Von Kármán rotating flow of Maxwell nanofluids featuring the Cattaneo-Christov theory with a Buongiorno model, Appl. Math. Mech. 41 (2020) 1195–1208.
[4] F. Mabood, A. Rauf, B.C. Prasannakumara, M. Izadi, S.A. Shehzad, Impacts of Stefan blowing and mass convention on flow of Maxwell nanofluid of variable thermal conductivity about a rotating disk, Chin. J. Phys. 71 (2021) 260–272.
[5] P. Sreedevi, P.S. Reddy, Effect of SWCNTs and MWCNTs Maxwell MHD nanofluid flow between two stretchable rotating disks under convective boundary conditions, Heat Tran. Asian Res. 48 (2019) 4105–4132.
[6] B.K. Siddiqui, S. Batool, Q.M. ul Hassan, M.Y. Malik, Irreversibility analysis in the boundary layer MHD two dimensional flow of Maxwell nanofluid over a melting surface, Ain Shams Eng. J. 12 (2021) 3217–3227.
[7] M. Khan, J. Ahmed, W. Ali, Thermal analysis for radiative flow of magnetized Maxwell fluid over a vertically moving rotating disk, J. Therm. Anal. Calorim. 143 (2021) 4081–4094.
[8] E. Osalusi, J. Side, R. Harris, Thermal-diffusion and diffusion-thermo effects on combined heat and mass transfer of a steady MHD convective and slip flow due to a rotating disk with viscous dissipation and Ohmic heating, Int. Commun. Heat Mass Tran. 35 (2008) 908–915.
[9] A. Ahmadian, M. Bilal, M.A. Khan, M.I. Asjad, Numerical analysis of thermal conductive hybrid nanofluid flow over the surface of a wavy spinning disk, Sci. Rep. 10 (2020), 18776.
[10] A. Ahmadian, M. Bilal, M.A. Khan, M.I. Asjad, The non-Newtonian maxwell nanofluid flow between two parallel rotating disks under the effects of magnetic field, Sci. Rep. 10 (2020), 17088.
[11] Y.X. Li, T. Muhammad, M. Bilal, M.A. Khan, A. Ahmadian, B.A. Pansera, Fractional simulation for Darcy-Forchheimer hybrid nanoliquid flow with partial slip over a spinning disk, Alex. Eng. J. 60 (2021) 4787–4796.
[12] X.H. Zhang, E.A. Algehyne, M.G. Alshehri, M. Bilal, M.A. Khan, T. Muhammad, The parametric study of hybrid nanofluid flow with heat transition characteristics over a fluctuating spinning disk, PLoS One 16 (2021), e0254457.
[13] S.S. Zhou, M. Bilal, M.A. Khan, T. Muhammad, Numerical analysis of thermal radiative maxwell nanofluid flow over-stretching porous rotating disk, Micromachines 12 (2021) 540.
[14] P.S. Reddy, P. Sreedevi, K.V.S. Rao, Impact of heat generation/absorption on heat and mass transfer of nanofluid over rotating disk filled with carbon nanotubes, Int. J. Numer. Methods Heat Fluid Flow 31 (2021) 2962–2985.
[15] S. Nazia, B. Seshaiah, P. Sreedevi, P.S. Reddy, Brownian motion and thermophoresis effect on heat and mass transfer of the Reiner–Rivlin nanofluid flow over a rotating disk with thermal radiation, Waves Random Complex Media (2022) 1–25.
[16] P.S. Reddy, P. Sreedevi, Heat and mass transfer analysis of single walled carbon nanotubes-water and multi wall carbon nanotubes-water based maxwell nanofluid flow over stretchable rotating disks, J. Nanofluids 12 (2023) 1151–1159.
[17] S. Nazia, B. Seshaiah, P.S. Reddy, P. Sreedevi, Silver–ethylene glycol and copper–ethylene glycol based thermally radiative nanofluid characteristics between two rotating stretchable disks with modified Fourier heat flux, Heat Transfer 52 (2023) 289–316.
[18] S. Kumar, K. Sharma, Impacts of Stefan blowing on Reiner–Rivlin fluid flow over moving rotating disk with chemical reaction, Arabian J. Sci. Eng. 48 (2023) 2737–2746.
[19] N. Vijay, Kushal Sharma, Entropy generation analysis in MHD hybrid nanofluid flow: effect of thermal radiation and chemical reaction, Numer. Heat Tran., Part B: Fundam. (2023) 1–17.
[20] S. Kumar, K. Sharma, Entropy optimization analysis of Marangoni convective flow over a rotating disk moving vertically with an inclined magnetic field and nonuniform heat source, Heat Transf 52 (2023) 1778–1805.
[21] N. Vijay, K. Sharma, Magnetohydrodynamic hybrid nanofluid flow over a decelerating rotating disk with Soret and Dufour effects, Multidisc, Mod. Mater. Struct. 19 (2023) 253–276.
[22] N. Vijay, K. Sharma, Dynamics of stagnation point flow of Maxwell nanofluid with combined heat and mass transfer effects: a numerical investigation, Int. Commun. Heat Mass Tran. 141 (2023), 106545.
[23] A.M. Alqahtani, M. Bilal, F.A.A. Elsebaee, S.M. Eldin, T.R. Alsenani, A. Ali, Energy transmission through carreau yasuda fluid influenced by ethylene glycol with activation energy and ternary hybrid nanocomposites by using a mathematical model, Heliyon 9 (2023), e14740.
[24] P.S. Reddy, P. Sreedevi, A.J. Chamkha, Magnetohydrodynamic (MHD) boundary layer heat and mass transfer characteristics of nanofluid over a vertical cone under convective boundary condition, Prop. Power Res. 7 4 (2018) 308–319.
[25] A. Hafeez, M. Khan, J. Ahmed, A. Ahmed, Z. Iqbal, Flow of Oldroyd-B fluid over a rotating disk through porous medium with Soret–Dufour effects, Arab, J. Sci. Eng. 45 (2020) 5949–5957.
[26] A. Hafeez, M. Khan, J. Ahmed, Stagnation point flow of radiative Oldroyd-B nanofluid over a rotating disk, Comp. Meth.Prog. Biomed. 191 (2020), 105342.
[27] S. Rosseland, Astrophysik und Atom-Theoretische Grundlagen, Springer Verlag, Berlin, 1931, pp. 41–44.
[28] M. Khan, A. Hafeez, J. Ahmed, Impacts of non-linear radiation and activation energy on the axisymmetric rotating flow of Oldroyd-B fluid, Phys. A: Stat. Mech. Appl. 580 (2021), 124085.
[29] F.S. Bayones, A.M. Abd-Alla, E.N. Thabet, Magnetized dissipative Soret effect on nonlinear radiative Maxwell nanofluid flow with porosity, chemical reaction and Joule heating, Waves Random Complex Media (2022) 1–19.
[30] A. Postelnicu, Influence of a magnetic field on heat and mass transfer by natural convection from vertical surfaces in porous media considering Soret and Dufour effects, Int. J. Heat Mass Tran. 47 (2004) 1467–1472.